

Comparative Study of InGaAs and GaAsSb Nanowires for Room Temperature Operation of Avalanche Photodiodes at 1.55 μm

Shrivatch Sankar, Punam Murkute, Micah Meleski, Nathan Gajowski, Neha Nooman, Md. Saiful Islam Sumon, Shamsul Arafin*, Ronald M. Reano, and Sanjay Krishna

Department of Electrical and Computer Engineering, The Ohio State University, Columbus, OH 43210, USA

*Corresponding author, email: arafin.1@osu.edu

Abstract

III-V semiconductor nanowire-based photodetectors have significant potential for remote sensing and LiDAR applications, particularly due to their ability to operate at 1.55 μm . Achieving room-temperature operation and near-unity absorption using these nanowires at 1.55 μm is crucial for single-photon detection, which offers a promising solution to the challenges posed by the existing superconducting nanowire single-photon detectors. Key materials suited for this wavelength include lattice-matched $\text{In}_{0.53}\text{Ga}_{0.47}\text{As}$ and $\text{Ga}_{0.5}\text{As}_{0.5}\text{Sb}$ to InP. This study reports a comparison between InGaAs and GaAsSb nanowires to achieve high absorption efficiency at room temperature. Through optimized nanowire arrangement and geometry, we aim to maximize absorption. Our approach features a comparative analysis of patterned InGaAs and GaAsSb nanowires with absorption characteristics modeled using finite-difference time-domain simulations to enhance absorption at the target wavelength. We also present the complete workflow for nanowire fabrication, modeling, and simulation, encompassing the production of tapered nanowire structures and measurement of their absorption efficiency. Our experimental results show that tapered InGaAs and GaAsSb nanowires exhibit an absorption efficiency of 93% and 92%, respectively, at room temperature around 1.55 μm .

Introduction

Quantum photodetectors, also known as single-photon detectors (SPDs), are increasingly in demand due to advancements in fields like quantum communication, quantum computing, quantum sensing, and metrology [1-6]. These applications have expanded rapidly within the broader scope of quantum information science (QIS), propelled by recent breakthroughs in photonic qubit technology, particularly the introduction of single-photon sources, such as single-photon emitters (SPEs) [7, 8]. This has further intensified the need for highly sensitive quantum photodetectors capable of efficient single-photon detection [9, 10]. This need is also reinforced by the recent developments in superconducting qubits, where optical transduction requires highly sensitive photodetectors to ensure reliable signal detection.

The short-wave infrared (SWIR) region of the electromagnetic spectrum plays an essential role in both classical and quantum telecommunications. Fiber optics, heavily utilized in these applications, exhibit ultra-low absorption losses in the SWIR range (~ 1560 nm), allowing for efficient long-distance transmission of single photons [11]. Quantum communication systems also leverage this range due to its support of low-loss, high-efficiency photon transmission over fiber, making it a prime choice for quantum information transfer [12-14]. Consequently, there has been a surge of interest in developing SWIR single-photon sources through various methods, including

crystal vacancies, higher-order harmonic generation, and quantum dots [8, 15-18]. At present, the superconducting nanowire single-photon detector (SNSPD) is regarded as the state-of-the-art technology for SWIR single-photon detection [19, 20]. SNSPDs rely on nanowire pillars made of thin-film superconductors operating at cryogenic temperatures between 2–5 K. When biased just below their critical current, an incident photon disrupts the nanowire’s superconductivity, generating a voltage pulse that marks a single-photon detection event.

Despite their effectiveness, SNSPDs face limitations in scalability due to their low-temperature operating requirements and susceptibility to environmental variations [21, 22]. By contrast, photonic qubits—operable at room temperature (RT)—offer a more robust, cost-effective alternative for large-scale quantum applications [23]. In this context, III-V semiconductor-based single-photon nanowire arrays present a compelling solution for RT single-photon detection, with properties such as high absorption coefficients, excellent carrier mobility, and lower dark current [24-26]. While single nanowire-based detectors have been widely investigated, they are constrained by limited optical efficiency [27]. Nanowire arrays, however, provided enhanced optical properties, including antireflective behavior and strong coupling of light along the nanowire axis, guiding resonant light efficiently and improving absorption [27, 28]. Tapering these nanowires further improves absorption by concentrating the electric field near their surfaces and reducing recombination losses, particularly around the C-band. This approach maximized the photodiode’s internal gain while minimizing noise, ultimately improving sensitivity and speed for effective single-photon detection [29-32].

This study focuses on the development of InGaAs and GaAsSb nanowire arrays required to eventually demonstrate highly-sensitive RT avalanche photodiodes operating in Geiger mode for quantum applications. In this paper, we provide detailed modeling and simulations results of nanowires using finite-difference time-domain (FDTD) techniques. Additionally, we discuss the fabrication processes and absorption measurements conducted on the resulting nanowire arrays. By refining the geometry and shape of the nanowire arrays, we designed a near-unity absorber capable of covering a broad spectrum from 1200 to 2500 nm, achieving an average calculated absorptance of 92%. Notably, the InGaAs nanowires exhibit near-unity absorption across the 900–2000 nm range, with an average absorption efficiency of 92%. A comparison with bulk InGaAs of similar thickness shows that the nanowire array’s geometry and configuration significantly enhance absorption, approaching unity. As a result, InGaAs and GaAsSb semiconductor nanowires offer a near-unity absorption at the target wavelength, providing an alternative to commercially available detectors in this wavelength range without the need for cryogenic cooling.

Experimental details:

Two 1400 nm-thick unintentionally doped samples of $\text{In}_{0.53}\text{Ga}_{0.47}\text{As}$ and $\text{GaAs}_{0.5}\text{Sb}_{0.5}$ were epitaxially grown on a semi-insulating, double-side polished InP substrate. The growth process utilized molecular beam epitaxy (MBE) in a RIBER Compact 21 DZ system. Both samples were deposited on the InP substrate at a temperature of 510°C. For the $\text{In}_{0.53}\text{Ga}_{0.47}\text{As}$ layer, the V/III flux ratio was maintained at 25, with an In/Ga flux ratio of 18 to achieve optimal material composition and crystalline quality. For $\text{GaAs}_{0.5}\text{Sb}_{0.5}$ growth, the temperature was kept constant at 485°C as well, while the As/Sb ratio was 4.7 and the III/V ratio was 17.4, designed to stabilize the Sb incorporation and achieve the desired stoichiometry. Both the as-grown planar structures were turned into tapered nanowires as shown in **Figure 1**.

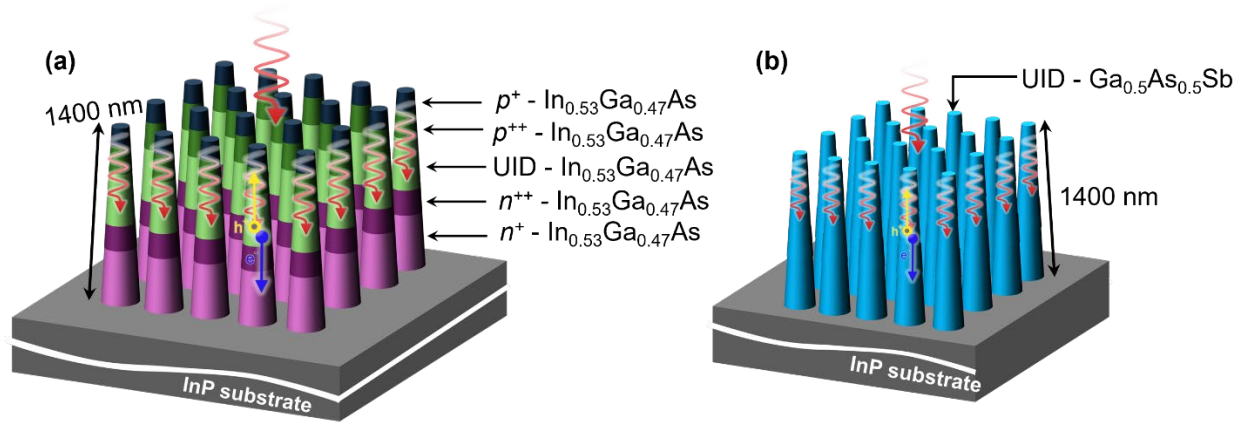


Figure 1: schematics of the tapered nanowire arrays based on UID- (a) $\text{In}_{0.53}\text{Ga}_{0.47}\text{As}$ (b) $\text{Ga}_{0.5}\text{As}_{0.5}\text{Sb}$ investigated in this study.

High-resolution X-ray diffraction (XRD) measurements were conducted using a Bruker D8 X-ray diffractometer equipped with a copper $\text{K}\alpha$ X-ray source and a Ge (004) monochromator in the incident optics. The XRD rocking curve measurements confirmed a good lattice match for the InGaAs and GaAsSb layer with respect to InP as shown in **Figures 2(a)** and **(b)**. The RT PL measurements were performed on both samples to confirm optical activity with minimal defect states and high optical quality. Both samples exhibited room temperature PL, with peaks at approximately 1690 nm and 1676 nm, as shown in **Figures 2(c)** and **(d)**. The surface morphology of the grown film was analyzed using a Bruker atomic force microscope (AFM) in tapping mode over a $5 \times 5 \mu\text{m}$ scan range. Uniform film deposition was observed for both samples, with surface roughness values of 2.1 Å for InGaAs and 3.7 Å for GaAsSb samples (see **Figures 2(e)** and **(f)**).

Electromagnetic modeling of the nanowires was performed using ANSYS Lumerical's Finite Difference Time Domain (FDTD) solver with periodic boundary conditions along the X and Y axes and Perfectly Matched Layer (PML) boundaries along the Z axis to avoid artificial reflections. InGaAs and GaAsSb material properties were modeled using Lumerical's curve-fit approximation, shown in **Figure 3**, based on experimentally measured n and k data. While initial data and previous work suggest that these nanowires perform well up to 400 nm [33], we limit this study to the 900-1800 nm wavelength range, reducing simulation time and improving material fit over this band of interest, noting that absorption is not expected for any of these materials above 1750 nm based on the measured bandgaps of these InGaAs and GaAsSb samples [34].

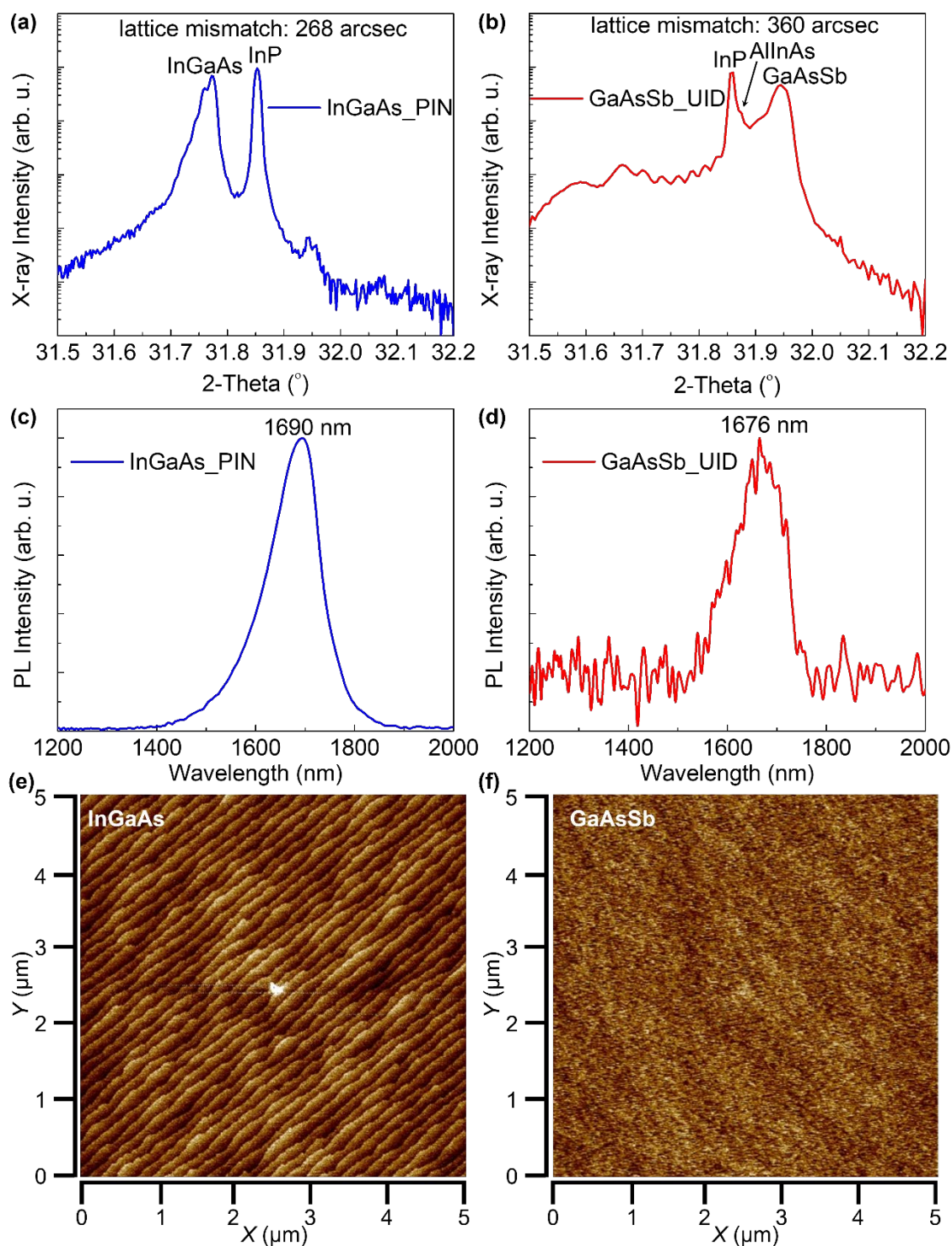


Figure 2: (a).-(b). High-resolution X-ray diffraction (XRD) peaks for epitaxially grown (a). InGaAs and (b). GaAsSb layers on InP substrate, demonstrating effective lattice matching with the InP substrate, confirming high crystalline quality, (c).-(d). display room temperature photoluminescence spectra for 1400 nm-thick (c). InGaAs and (d). GaAsSb layer, (e).-(f). illustrate

surface quality assessments of the (e). InGaAs and (f). GaAsSb layers, respectively, obtained through atomic force microscopy (AFM).

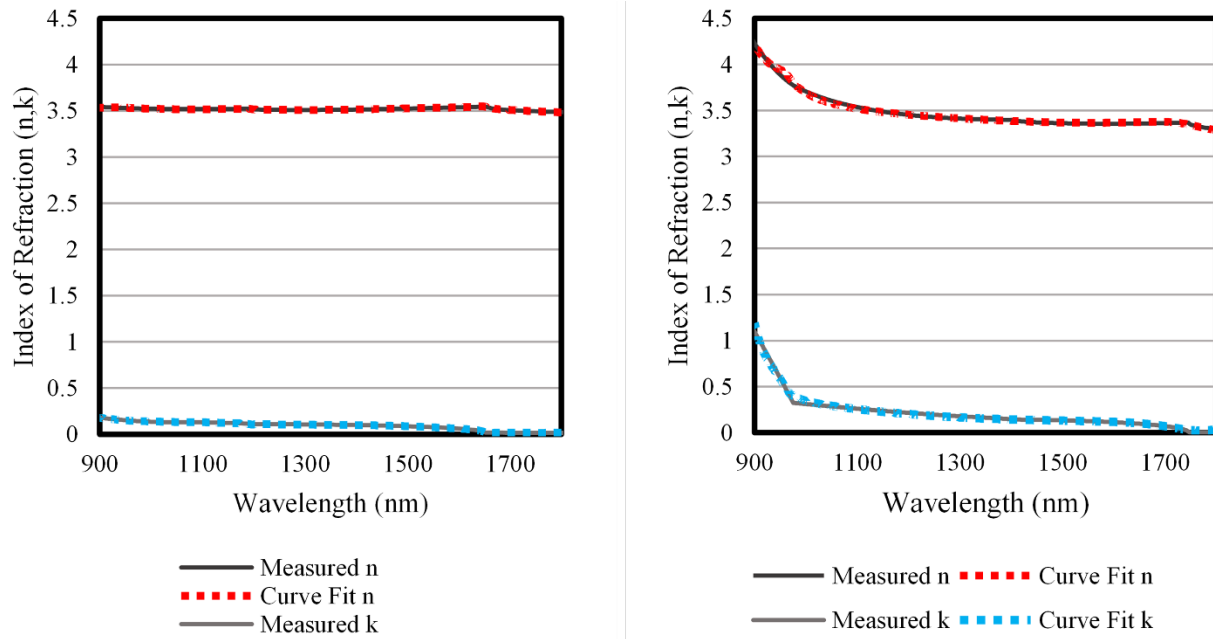


Figure. 3: Material curve fit approximations compared to their measured data sources for (a) InGaAs and (b) GaAsSb.

Results and Discussions:

a). Tapered Nanowire Simulations

Geometry sweeps of GaAsSb and InGaAs tapered nanowires in air were performed by varying the length L , top radius r_t , bottom radius r_b , and pitch p . Each parameter was initially varied over a broad range and then refined to determine the optimal dimensions. As an initial point of reference, we borrowed the geometry from Tekcan et al. based on its notable performance, noting that the n and k are generally similar between our GaAsSb and Tekcan's InGaAs over the wavelength range of interest [2]. However, using our own measured data for InGaAs, we observed a substantial decrease in performance, with absorptance near 70% at 1550 nm, noting that our measured k is significantly lower than Tekcan's [2]. Results are shown in **Figures 4a & 4b**, with high absorption at shorter wavelengths. To improve absorption at the target wavelength, the nanowire size and pitch were increased to better excite a leaky mode resonance near the bandgap of these materials. Further discussion of the parametric sweep of nanowire geometry can be found in the supplementary notes, Section SX. From these parametric sweeps, a final geometry of $Z=1600\text{nm}$, $p=1050\text{nm}$, $r_b=490\text{nm}$, and $r_t=260\text{nm}$ was selected for the tapered nanowire. The absorption for this geometry is shown below in **Figure. 4c** and **4d**, exhibiting favorable performance with both InGaAs and GaAsSb materials.

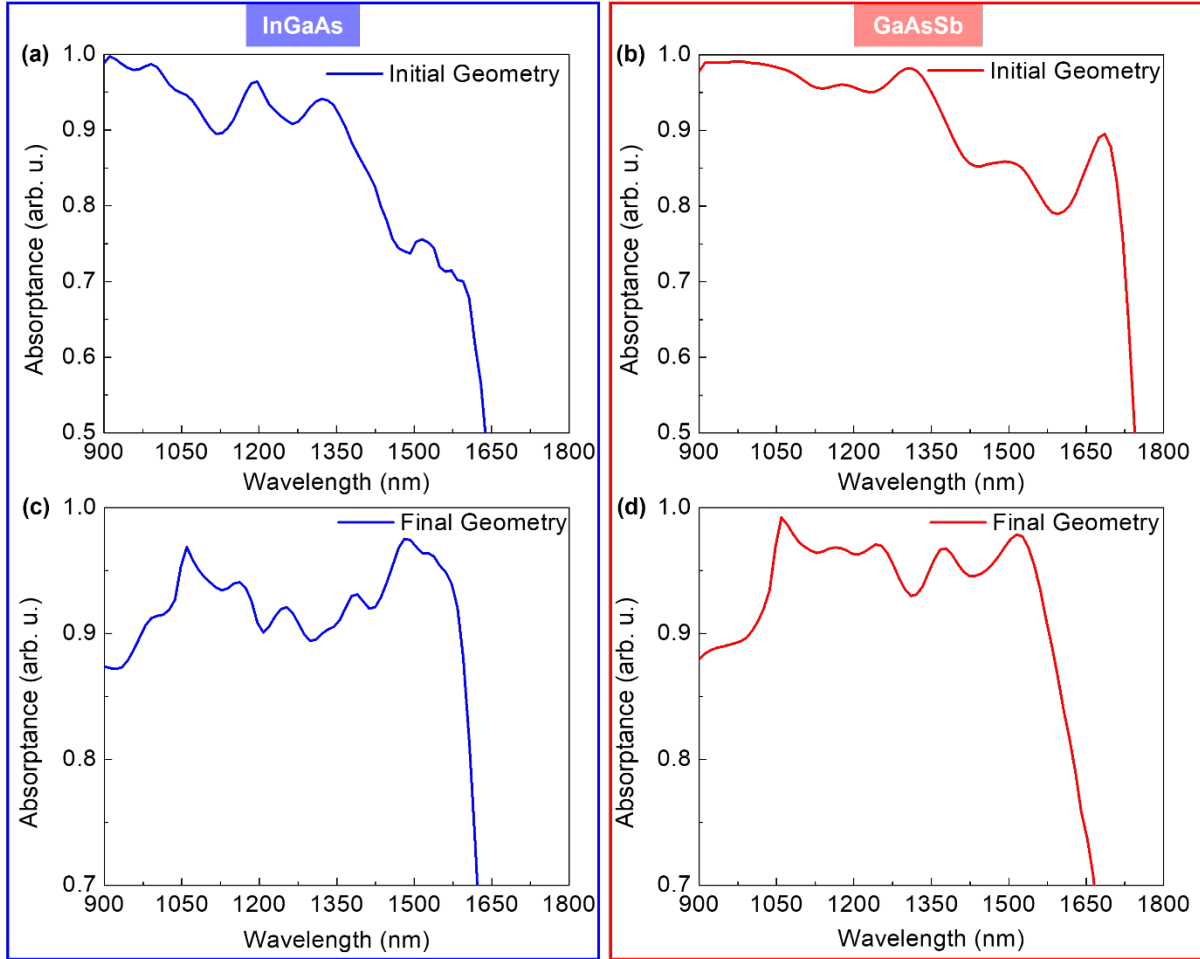


Figure 4, (4a) & (4b) displays the initial tapered nanowire absorption. **(a).** InGaAs, **(b).** GaAsSb ($L = 1400\text{nm}$, $p = 900\text{nm}$, $r_t = 170\text{nm}$, $r_b = 441\text{nm}$), **(4c) & (4d)** Tapered nanowire absorption for proposed geometry, **(c).** InGaAs, **(d).** GaAsSb

b). Substrate Impact on Absorption

With an initial geometry developed, the impact of the substrate was then considered by comparing the absorption of the tapered nanowires directly on an InP substrate with the absorption of the tapered nanowires featuring a GaAsSb layer atop an InP substrate. Tapered nanowires directly mounted on InP showed substantially decreased absorption at higher wavelengths as shown in **Figure 5a**. This phenomenon arises from the relatively low refractive index contrast between the nanowire material and the InP substrate, which facilitates light propagation into the substrate and enhances the transmittance of the metamaterial structure (see Supplementary Notes SY for visualizations of the electric field). Increasing the thickness of the GaAsSb layer gradually recovered performance at longer wavelengths, with shorter wavelengths showing improved absorption compared to the initial values without a substrate. InGaAs exhibited similar behavior, albeit with lower total absorption as displayed in **Figure 5b**.

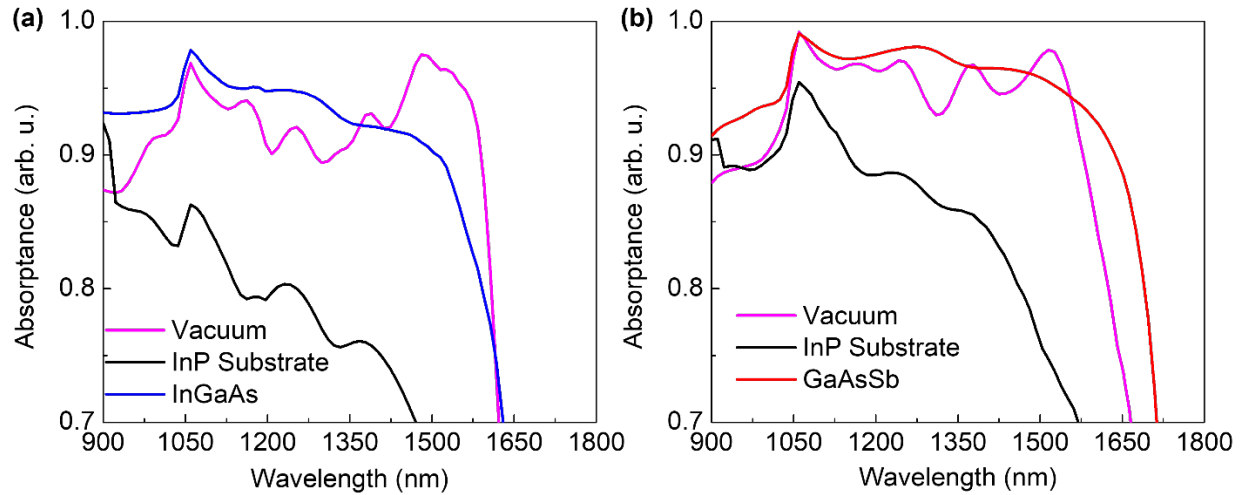


Figure 5, absorption of tapered nanowires in vacuum, with substrate, and with a 1400nm thick layer of (a) InGaAs, (b) GaAsSb separating the tapered nanowires from the InP substrate.

While it is possible to recover and potentially improve absorption with a substantial layer of GaAsSb, cylindrical nanowires were considered as a narrow-band solution with reduced surface area contact to the InP substrate. In an identical test to the tapered nanowire case, cylindrical nanowires with a radius of 170 nm demonstrated significantly improved absorption when mounted directly onto the InP substrate, although they did not exhibit broad-band absorption in this configuration. However, at a slab thickness of 900 nm, broadband performance notably improved, particularly for GaAsSb. **Figures 6a** and **6b** show a comparison between cylindrical and tapered nanowires when directly mounted to the substrate, as well as at a material slab thickness of 1400 nm for both cases, InGaAs and GaAsSb. The supplementary section (SZ) contains swept plots comparing GaAsSb cylindrical nanowires with tapered nanowires as a function of slab thickness, illustrating the behavior of increasing slab thickness for both tapered and cylindrical cases. From these results, both tapered and cylindrical nanowires offer viable options for near-unity absorption, though each configuration involves design trade-offs. Among the two materials simulated, GaAsSb demonstrated stronger absorption for both geometries.

c). Performance Prediction of Fabricated Nanowires and Tapered Nanowires

The materials team has fabricated cylindrical nanowires and tapered nanowires of both InGaAs and GaAsSb, depicted schematically in Supplementary notes SZA. These nanowire geometries were simulated from 900-1800nm to predict performance. From **Figures 6c** and **6d**, the improved performance of both the GaAsSb and the tapered nanowire to the cylindrical nanowire is noted. Further iteration will be conducted to create an optimized, manufacturable nanowire geometry for enhanced absorption.

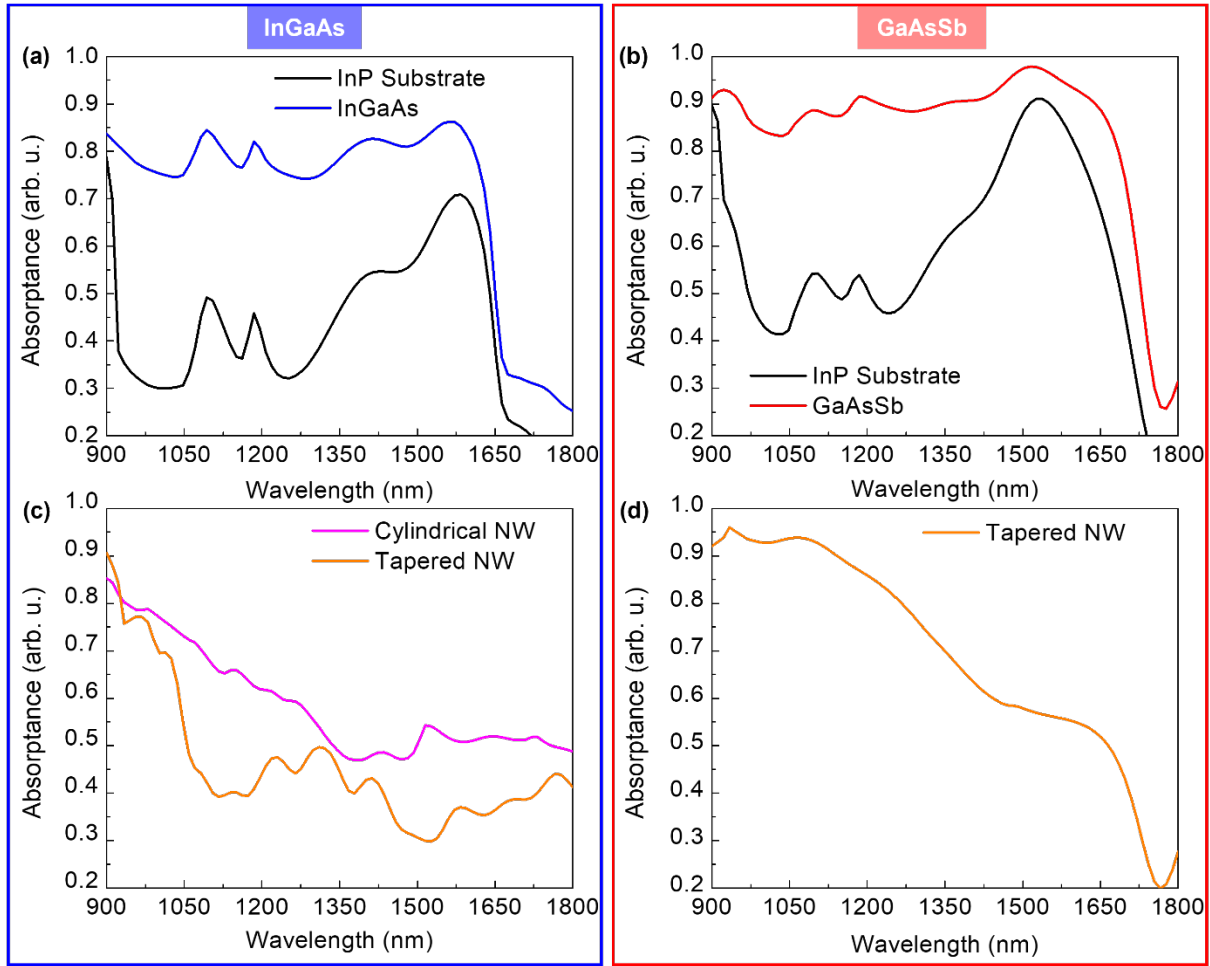


Figure. 6a and 6b, Absorption of tapered vs cylindrical nanowires, mounted on an InP substrate, with and without an intermediate bulk layer of material. **(a)** InGaAs, **(b)** GaAsSb. **6c and 6d**, Predicted absorption of fabricated tapered nanowires and cylindrical nanowires in **(c)** InGaAs and **(d)** GaAsSb.

d). Fabrication:

As discussed in the modeling section, NWs were designed in different configurations: cylindrical and tapered, as shown in **Figure 6c and 6d**. To fabricate these designs, 1400 nm-thick as-grown InGaAs on an InP substrate *p-i-n* sample and 1400 nm-thick UID GaAsSb were used. The fabrication process was planned to focus first on the formation of cylindrical nanowires, followed by the optimization of the dry etch recipe to taper the nanowires, achieving the desired dimensions. The fabrication process flow is shown in **Figure 7**. To form the cylindrical nanowires, electron beam lithography (EBL) was employed for patterning, as the nanowire diameter was 340 nm, which conventional photolithography cannot handle. Since the e-beam resist cannot withstand the III-V plasma etching, a 200 nm-thick silicon dioxide (SiO₂) hard mask was deposited on top of the InGaAs and GaAsSb samples. This SiO₂ layer acts as a mask during the III-V etching process. Among various e-beam resists considered for nanowire fabrication, maN-2403 negative-tone resist was selected because its negative-tone properties reduce the EBL patterning time. The thickness of maN-2403 was chosen to be approximately 300 nm to enhance the selectivity during hard mask etching. After exposure, the sample was developed using MF-319

developer, followed by SiO₂ hard mask etching. For the SiO₂ etching, Inductively Coupled Plasma Reactive Ion Etching (ICP-RIE) dry etching was used with CF₄/CHF₃ plasma, which interacts only with silicon-based materials, thereby protecting the surfaces of InGaAs and GaAsSb.

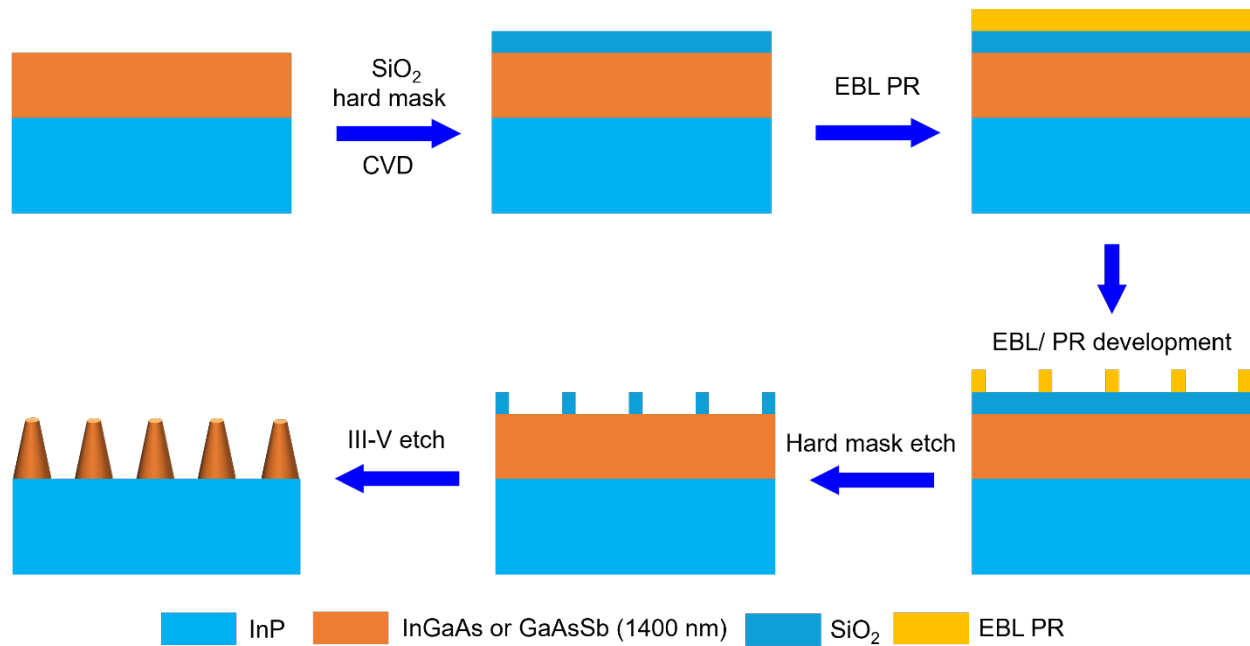


Figure 7. Detailed process flow of InGaAs or GaAsSb nanowire fabrication.

The III-V materials were etched using ICP-RIE technology with a CH₄/H₂/Cl₂ plasma. Initially, cylindrical InGaAs nanowires were etched with a chamber pressure of 20 mTorr, an RF power of 85 W, and an ICP power of 750 W at a high temperature of 180°C to avoid the formation of InCl_x. Under these conditions, the SiO₂ hard mask was etched for 4 minutes. After etching, the sample was immersed in a buffered oxide etch (BOE) solution to remove the remaining SiO₂ mask. Subsequent SEM analysis revealed that the etch profile was cylindrical, as expected, with an etch depth of 1800 nm, as shown in **Figure 8(a)**. This also indicates that 400 nm of the InP substrate was etched during the process. After fabricating the cylindrical nanowires, the focus shifted to creating tapered nanowires. Initial attempts aimed at achieving a taper angle of 79° involved varying the RF and ICP power while keeping the gas flow and pressure constant. However, these attempts resulted in cylindrical nanowires with reduced etch rates. The approach was then adjusted by maintaining constant ICP/RF power and gas flows while lowering the pressure from 20 mTorr to 5 mTorr. This adjustment successfully produced tapered nanowires with a taper angle of approximately 77° (close to the desired 79°), as shown in **Figure 8(b)**, with an etch rate of 252 nm/min and an etch depth of 1180 nm. From the SEM data shown in Figures 10(a) and 10(b), we can visually confirm that the nanowire pillars have smooth sidewalls. This is important, as roughness in the sidewalls could potentially lead to increased surface recombination and affect absorption due to light scattering. Following the fabrication of the InGaAs nanowires, we shifted our focus to GaAsSb nanowires. When using the same recipe as for the InGaAs cylindrical nanowires, we obtained a sloped profile, as shown in the SEM image in **Figure 8(c)**, with an etch depth of 990 nm and a slope angle of 83°. Interestingly, the GaAsSb nanowires showed rough sidewalls with visible cracks. This suggests that the chlorine flow should be more carefully adjusted to achieve smoother sidewalls in GaAsSb nanowires.

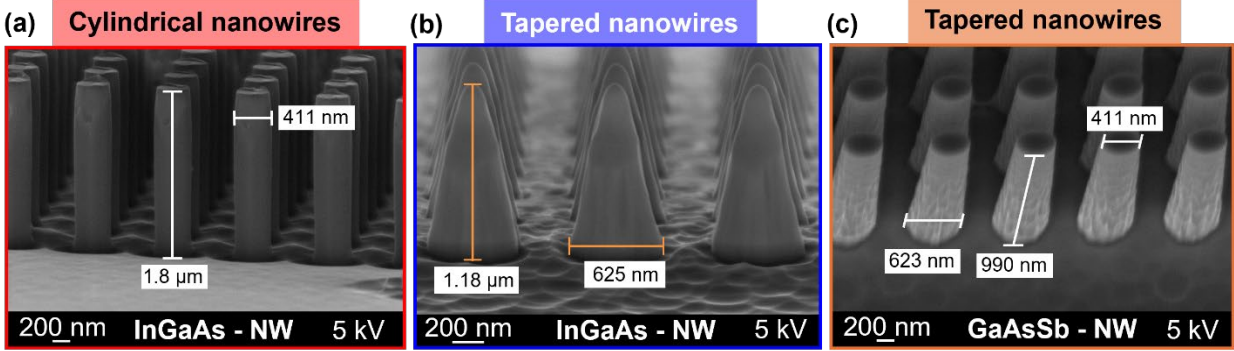


Figure. 8, displays (a). Formation of InGaAs cylindrical nanowires, (b). Formation of InGaAs tapered nanowires with a taper angle of 77° , (c). Formation of GaAsSb tapered nanowires with a taper angle of 83° .

e). Absorption efficiency Measurement

Absorption measurements on the fabricated nanowires were performed using an iZ10/Right AEM Thermo Fisher microscope and an iS50R FTIR spectrometer at room temperature. The sample was mounted on an IR-opaque stage, and the substrate alone was recorded as the background. Measurements were taken for the epitaxial material on the substrate in both transmission and reflection modes. Reflectance data was adjusted to absolute reflectance using a gold standard, while transmission data was corrected by subtracting the background (i.e., the substrate). Final absorption was calculated using $T+R+A=1$, where T is transmission, R is reflectance, and A is absorption.

The tapered geometry of InGaAs nanowires significantly enhanced absorption efficiency, especially across the long-wavelength range. Tapered and cylindrical nanowires showed high absorption efficiencies, achieving around 92% at room temperature at a wavelength of $1.76 \mu\text{m}$. GaAsSb nanowires exhibited an absorption efficiency of approximately 91% at $1.48 \mu\text{m}$. Although both materials displayed similar PL peak intensities around $1.6 \mu\text{m}$, the peak absorption efficiencies differed, with InGaAs and GaAsSb peaking at $1.76 \mu\text{m}$ and $1.48 \mu\text{m}$, respectively. This indicates that nanowire absorption characteristics are strongly influenced by geometry, underscoring its critical role in absorption efficiency. By adjusting nanowire geometry, we can fine-tune the operational wavelength to meet specific targets, with additional optimization required to align InGaAs absorption efficiency precisely at the $1.55 \mu\text{m}$ wavelength range.

Notably, the fabricated tapered nanowire structures demonstrated superior absorption efficiency compared to bulk InGaAs films (**Figure. 9c**).

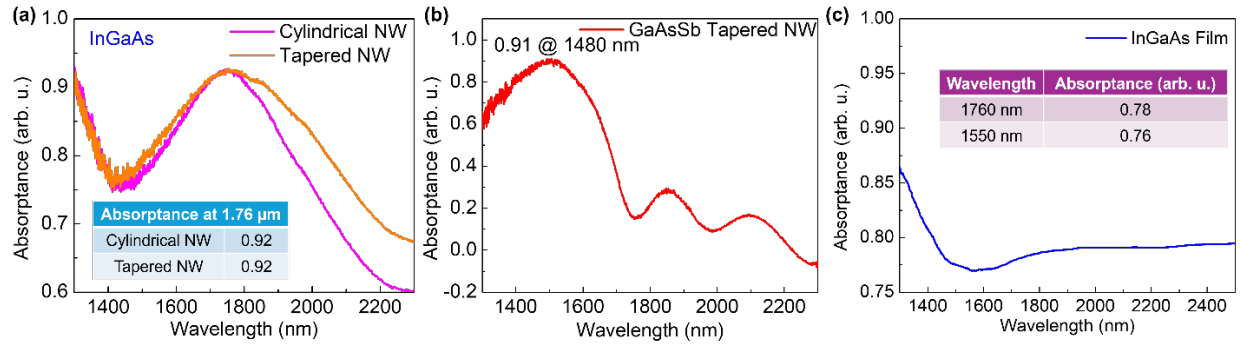


Figure. 9 Percentage absorption measured in fabricated nanowire (a) InGaAs NW with the cylindrical and tapered array, (b) GaAsSb NW with tapered nanowire array, (c) InGaAs film absorption with nanowire fabrication.

To demonstrate the enhanced absorption in tapered nanowires, we compared it to an unprocessed bulk InGaAs film with a thickness of 1400 nm. The measured bulk InGaAs film absorbance is shown as a function of wavelength in **Figure. 9c** (blue solid curve). The absorption enhancement towards unity when utilizing the tapered nanowire geometry is evident when comparing tapered nanowires (**Figure. 9a**) and the planar bulk material. Numerical calculations and the measured performance for a series of varied nanowire geometries were also studied. Despite deviating from the optimized structure, our measurements show the reproducibility of enhanced absorption in tapered nanowires.

To highlight the enhanced absorption in tapered nanowire, we compared them to an unprocessed bulk InGaAs film with a thickness of 1400 nm. The bulk film's absorption as a function of wavelength is displayed in Fig. 11c (blue solid curve). The absorption enhancement in the tapered nanowire geometry approaches unity, as shown by comparing tapered nanowires (**Figure. 11a**) with the planar bulk material (**Figure. 9c**). Numerical calculations and experimental performance for varied nanowire geometries further confirmed the reproducibility of this enhanced absorption in tapered nanowires, even when deviating slightly from the optimized structure.

Conclusion:

This study demonstrates the successful design, fabrication, and performance characterization of tapered InGaAs and GaAsSb nanowires, with a focus on achieving near-unity absorption efficiency. By optimizing the geometry of the nanowires using finite-difference time-domain (FDTD) simulations, we were able to significantly enhance the absorption efficiency of both materials, especially in the short wave-infrared (SWIR) range. The tapered InGaAs nanowires exhibited an absorption efficiency of approximately 93%, while the GaAsSb nanowires achieved an absorption efficiency of 91%, both significantly outperforming bulk material absorbance. The tapered geometry proved particularly effective in improving absorption across a broad wavelength range, with a significant enhancement over conventional cylindrical nanowires. This highlights the critical role of nanowire geometry in optimizing photodetector performance. Through the fabrication process, including the use of electron beam lithography (EBL) and precise control over etching conditions, we demonstrated reproducible and high-quality tapered nanowire structures. The results confirm the potential of tapered semiconductor nanowires for applications in advanced

photonics, particularly in quantum photodetection, where high absorption efficiency and sensitivity to near-infrared photons are crucial. This work offers new insights into the design of nanowire arrays for photodetectors, paving the way for developing highly efficient and scalable quantum photonic devices that do not require cryogenic cooling.

References

- [1] L. de Forges de Parny *et al.*, “Satellite-based quantum information networks: use cases, architecture, and roadmap,” *Communications Physics*, vol. 6, no. 1, p. 12, 2023.
- [2] A. M. Zagoskin *et al.*, “Spatially resolved single photon detection with a quantum sensor array,” *Scientific reports*, vol. 3, no. 1, p. 3464, 2013.
- [3] J. L. O’Brien, “Optical quantum computing,” *Science*, vol. 318, no. 5856, pp. 1567-1570, 2007.
- [4] R. H. Hadfield, “Single-photon detectors for optical quantum information applications,” *Nature photonics*, vol. 3, no. 12, pp. 696-705, 2009.
- [5] C. Couteau *et al.*, “Applications of single photons in quantum metrology, biology and the foundations of quantum physics,” *Nature Reviews Physics*, vol. 5, no. 6, pp. 354-363, 2023.
- [6] C. J. Chunnillall, I. P. Degiovanni, S. Kück, I. Müller, and A. G. Sinclair, “Metrology of single-photon sources and detectors: a review,” *Optical Engineering*, vol. 53, no. 8, pp. 081910-081910, 2014.
- [7] S. Gupta, W. Wu, S. Huang, and B. I. Yakobson, “Single-photon emission from two-dimensional materials, to a brighter future,” *The Journal of Physical Chemistry Letters*, vol. 14, no. 13, pp. 3274-3284, 2023.
- [8] S. Castelletto *et al.*, “A silicon carbide room-temperature single-photon source,” *Nature materials*, vol. 13, no. 2, pp. 151-156, 2014.
- [9] W. Luo *et al.*, “Recent progress in quantum photonic chips for quantum communication and internet,” *Light: Science & Applications*, vol. 12, no. 1, p. 175, 2023.
- [10] J. Zhang, M. A. Itzler, H. Zbinden, and J.-W. Pan, “Advances in InGaAs/InP single-photon detector systems for quantum communication,” *Light: Science & Applications*, vol. 4, no. 5, pp. e286-e286, 2015.
- [11] T. Hasegawa, Y. Tamura, H. Sakuma, Y. Kawaguchi, Y. Yamamoto, and Y. Koyano, “The first 0.14-dB/km ultra-low loss optical fiber,” *SEI Tech. Rev.*, vol. 86, pp. 18-22, 2018.
- [12] X. Wang *et al.*, “Tunable narrowband perfect absorption and active phase transition driven by gain-coupled bound states in the continuum: A basis for sensing,” *Physical Review Applied*, vol. 22, no. 5, p. 054002, 2024.
- [13] A. Dibos, M. Raha, C. Phenicie, and J. D. Thompson, “Atomic source of single photons in the telecom band,” *Physical review letters*, vol. 120, no. 24, p. 243601, 2018.
- [14] N. Sangouard and H. Zbinden, “What are single photons good for?,” *Journal of Modern Optics*, vol. 59, no. 17, pp. 1458-1464, 2012.
- [15] F. Lenzini, N. Gruhler, N. Walter, and W. H. Pernice, “Diamond as a platform for integrated quantum photonics,” *Advanced Quantum Technologies*, vol. 1, no. 3, p. 1800061, 2018.
- [16] P. Senellart, G. Solomon, and A. White, “High-performance semiconductor quantum-dot single-photon sources,” *Nature nanotechnology*, vol. 12, no. 11, pp. 1026-1039, 2017.
- [17] S. Scheel, “Single-photon sources—an introduction,” *Journal of Modern Optics*, vol. 56, no. 2-3, pp. 141-160, 2009.

- [18] L. Caspani *et al.*, “Integrated sources of photon quantum states based on nonlinear optics,” *Light: Science & Applications*, vol. 6, no. 11, pp. e17100-e17100, 2017.
- [19] F. Marsili *et al.*, “Detecting single infrared photons with 93% system efficiency,” *Nature Photonics*, vol. 7, no. 3, pp. 210-214, 2013/03/01 2013, doi: 10.1038/nphoton.2013.13.
- [20] C. M. Natarajan, M. G. Tanner, and R. H. Hadfield, “Superconducting nanowire single-photon detectors: physics and applications,” *Superconductor science and technology*, vol. 25, no. 6, p. 063001, 2012.
- [21] I. Holzman and Y. Ivry, “Superconducting nanowires for single-photon detection: progress, challenges, and opportunities,” *Advanced Quantum Technologies*, vol. 2, no. 3-4, p. 1800058, 2019.
- [22] M. Castellani *et al.*, “Nanocryotron ripple counter integrated with a superconducting nanowire single-photon detector for megapixel arrays,” *Physical Review Applied*, vol. 22, no. 2, p. 024020, 08/08/ 2024, doi: 10.1103/PhysRevApplied.22.024020.
- [23] I. Charaev *et al.*, “Single-photon detection using large-scale high-temperature MgB₂ sensors at 20 K,” *Nature Communications*, vol. 15, no. 1, p. 3973, 2024.
- [24] A. Restelli, J. C. Bienfang, and A. L. Migdall, “Single-photon detection efficiency up to 50% at 1310 nm with an InGaAs/InP avalanche diode gated at 1.25 GHz,” *Applied Physics Letters*, vol. 102, no. 14, 2013.
- [25] H. Wang *et al.*, “Emerging Single-Photon Detectors Based on Low-Dimensional Materials,” *Small*, vol. 18, no. 5, p. 2103963, 2022.
- [26] C. Liu, H.-F. Ye, and Y.-L. Shi, “Advances in near-infrared avalanche diode single-photon detectors,” *Chip*, vol. 1, no. 1, p. 100005, 2022.
- [27] Z. Li, J. Allen, M. Allen, H. H. Tan, C. Jagadish, and L. Fu, “Review on III-V semiconductor single nanowire-based room temperature infrared photodetectors,” *Materials*, vol. 13, no. 6, p. 1400, 2020.
- [28] R. LaPierre, M. Robson, K. Azizur-Rahman, and P. Kuyanov, “A review of III–V nanowire infrared photodetectors and sensors,” *Journal of Physics D: Applied Physics*, vol. 50, no. 12, p. 123001, 2017.
- [29] T. Bartschmid, F. J. Wendisch, A. Farhadi, and G. R. Bourret, “Recent advances in structuring and patterning silicon nanowire arrays for engineering light absorption in three dimensions,” *ACS Applied Energy Materials*, vol. 5, no. 5, pp. 5307-5317, 2021.
- [30] F. J. Wendisch *et al.*, “Morphology-graded silicon nanowire arrays via chemical etching: Engineering optical properties at the nanoscale and macroscale,” *ACS applied materials & interfaces*, vol. 12, no. 11, pp. 13140-13147, 2020.
- [31] J. Xin-Yang *et al.*, “Enhanced absorption of infrared light for quantum wells in coupled pillar-cavity arrays,” *Optics Express*, vol. 31, no. 5, pp. 7090-7102, 2023.
- [32] T. Khudiyev, E. Huseyinoglu, and M. Bayindir, “Non-resonant Mie scattering: Emergent optical properties of core-shell polymer nanowires,” *Scientific Reports*, vol. 4, no. 1, pp. 1-10, 2014.
- [33] B. Tekcan *et al.*, “Semiconductor nanowire metamaterial for broadband near-unity absorption,” *Sci Rep*, vol. 12, no. 1, p. 9663, Jun. 2022, doi: 10.1038/s41598-022-13537-y.
- [34] N. Anttu, H. Mäntynen, A. Sorokina, J. Turunen, T. Sadi, and H. Lipsanen, “Applied electromagnetic optics simulations for nanophotonics,” *Journal of Applied Physics*, vol. 129, no. 13, p. 131102, Apr. 2021, doi: 10.1063/5.0041275.

- [35] K. Yee, "Numerical solution of initial boundary value problems involving Maxwell's equations in isotropic media," *IEEE Transactions on antennas and propagation*, vol. 14, no. 3, pp. 302-307, 1966.
- [36] "Calculating absorbed optical power - higher accuracy. ANSYS Optics. (n.d.-a). <https://optics.ansys.com/hc/en-us/articles/360034915693-Calculating-absorbed-optical-power-Higher-accuracy> . ."